ACS PHYSICAL CHEMISTRY Au
AN OPEN ACCESS JOURNAL OF THE AMERICAN CHEMICAL SOCIETY

Understanding (La,Sr)(Co,Fe)$O_{3-\delta}$ Phase Instability within SOECs Using a Combined Experimental and Atomistic Modeling Approach

Heather S. Slomski, Jonas L. Kaufman, Michael J. Dzara, Nicholas A. Strange, Cameron Priest, Jeremy L. Hartvigsen, Nicholas Kane, Micah Casteel, Brandon C. Wood, David S. Ginley, Kyoung E. Kweon,* Brian P. Gorman,* and Sarah Shulda*

Cite This: *ACS Phys. Chem Au* 2025, 5, 207−218

Read Online

ACCESS | Metrics & More | Article Recommendations | Supporting Information

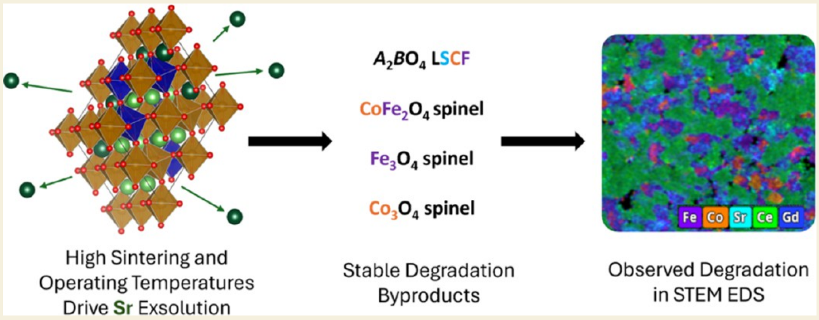

ABSTRACT: Understanding the onset of degradation in the air electrode within solid oxide electrolysis cells (SOECs), and the subsequent impact on cell performance, is a critical step in mitigating the performance losses and stability issues of SOECs. In an effort to identify early onset degradation phenomena, SOECs were characterized as fabricated and after testing potentiostatically at 1.3 V for 1000 h at 750 °C. SOEC air electrodes composed of a 1:1 composite of $La_{0.6}Sr_{0.4}Co_{0.2}Fe_{0.8}O_{3-\delta}$ (6428-LSCF) and $Gd_{0.1}Ce_{0.9}O_{1.95}$ (GDC) were studied using synchrotron X-ray diffraction (XRD), scanning transmission electron microscopy coupled with energy dispersive X-ray spectroscopy (STEM-EDS), and X-ray absorption near-edge spectroscopy (XANES) to evaluate the changes in the air electrode structurally and chemically. These techniques show the migration of Sr species from the air electrode through pores in the GDC barrier layer, progressing to the electrolyte boundary, where it accumulates and reacts with $(Zr_{0.84}Y_{0.16})O_{2-\delta}$ (YSZ) to form $SrZrO_3$. Microscopy results are paired with atomistic simulations to better understand the relationship between the thermodynamic instability of 6428-LSCF and cell fabrication/testing conditions. First-principles calculations reveal that LSCF-6428 is not stable during cell manufacturing and testing conditions, which supports the experimental identification of secondary phases in both as-fabricated and tested cells. Together, these results demonstrate that the challenging environments encountered by SOECs during cell manufacturing and operation lead to instabilities of the target 6428-LSCF anode material and underscore the need for more durable, high-performing SOEC components.

KEYWORDS: *solid oxide electrolysis, LSCF, electrode degradation, microscopy, phase stability modeling*

■ INTRODUCTION

High-temperature electrolysis (HTE) is a promising technology for the hydrogen production industry. Solid oxide electrolysis cells (SOECs) operate at significantly higher temperatures than their lower-temperature counterparts, polymer or alkaline electrolysis cells, producing higher thermodynamic efficiencies without requiring precious metal catalysts.[1−3] SOECs can be paired with excess heat and energy sources (e.g., solar, nuclear plants, engine exhaust gas, biomass incinerators, or geothermal), making the process versatile for integration with existing industries.[4−7] Process system analysis has demonstrated that integrating HTE with excess heat sources can reduce the energetic and financial cost of clean hydrogen production, approaching the DOE Hydrogen Earthshot goals of \$1/kg.[8] However, challenges with durability limit the functional lifetimes of SOECs. Gaining an in-depth understanding of the relationship between material degradation and cell performance loss is crucial to modifying materials, processes, and operating conditions to improve the long-term durability of SOECs needed for widespread industry adoption.

One well-known durability issue is the degradation of the air electrode under high-temperature sintering and operating

Received: November 6, 2024
Revised: December 21, 2024
Accepted: December 27, 2024
Published: January 10, 2025

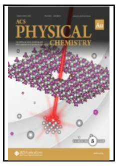

conditions, including secondary phase formation, segregation, and delamination.[9−20] The air electrode requires a material with both sufficiently high electronic and ionic conductivities in order to facilitate the oxygen evolution reaction.[21−24] $La_{0.6}Sr_{0.4}Co_{0.2}Fe_{0.8}O_{3-\delta}$ (6428-LSCF) is a commonly used air electrode material that has been extensively studied due to its high ionic and electronic conductivities.[13,25] Based on the perovskite $LaFeO_3$, Sr and Co are substituted on the A and B sites, respectively, to optimally tune conductivity. Sr^{2+} substitution on the La^{3+} A site causes oxygen vacancies to form within LSCF, promoting oxygen ion conductivity. The presence of oxygen vacancies and the imbalance of A and B site substitution in 6428-LSCF cause some Fe and Co to oxidize to a 4+ state, in turn increasing electronic conductivity.[26] Although 6428-LSCF has demonstrated high performance, it suffers from durability issues that inhibit lifetime hydrogen production capacity.[14,21,27−29]

While the chosen 6428-LSCF structure and composition is stoichiometrically stable at room temperature, it begins to show the formation of secondary phases accompanied by a subsequent decrease in electronic and ionic conductivity when temperatures exceed 600 °C.[13,25] The instability of 6428-LSCF near 600 °C proves problematic as sintering temperatures often exceed 900 °C and operating temperatures are near 750 °C for potentially >50,000 h. Previously, Tai et al.[13] observed that 6428-LSCF decreases in electrical conductivity above 550 °C, which they correlated to changes in oxygen vacancy concentration, B-site oxidation state, and thermal expansion. No significant secondary phases were observed by using X-ray diffraction (XRD), although phases could have been present below the detection threshold of the instrument. Tai et al. also observed that reducing Sr concentrations to a mole fraction less than 0.1 in LSCF (e.g., 9128-LSCF) showed no decreases in conductivity up to 1000 °C. Early data on LSCF, therefore, may have demonstrated that different LSCF stoichiometries have different ranges of thermodynamic stability, even if they were not detectable with XRD at the time.

Tracking the spatial distribution of unintended secondary phases as they form and potentially migrate across the cell (the cell composition schematic is shown in Figure 1) is crucial to understanding cell performance loss. As noted earlier, 6428-LSCF is known to exsolve Sr at temperatures above 600 °C, leading to mobile Sr throughout the cell.[10,25,30−32] Besides effects on the active Sr-deficient LSCF material, Sr secondarily becomes problematic as it can react with $(Zr_{0.84}Y_{0.16})O_{2-\delta}$ (YSZ), creating $SrZrO_3$ which can inhibit ionic conductivity.[10,25,33] Previous button cell testing results have found a reaction between Sr and Zr at the YSZ interface to form $SrZrO_3$ despite the presence of a GDC barrier layer. $SrZrO_3$ can lead to mechanical delamination and therefore SOEC performance degradation.[10,12,14,25,34,35] Gadolinium-doped ceria (GDC) barrier layers are used between the electrode and electrolyte in an attempt to mitigate cation migration and reduce secondary phase formation.[36−38] Additionally, GDC needs to be mixed into the LSCF to minimize thermal expansion stresses with the YSZ, hence the commonly used electrode composite LSCF/GDC 1:1.[11,39−41] However, the GDC layer itself presents additional complications as it introduces an additional possibility for reaction with degradation byproducts during sintering and cell testing.[11,27,42] Even considering these concerns, 6428-LSCF has been found to outperform other popular electrode materials.[25,43,44] Thus, it is an ideal model system to focus on for developing a robust understanding of the underlying degradation mechanisms currently impeding the long-term stability of LSCF-based anodes.

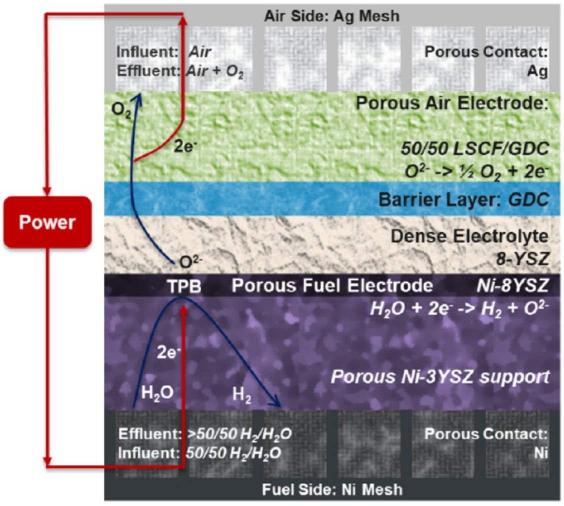

Figure 1. Schematic illustrating the composition and design of the SOEC samples analyzed.

In this study, we characterized structural and compositional changes in SOEC air electrodes to discriminate degradation between cell fabrication steps and early stages (1000 h) of operation. Synchrotron XRD, electron microscopy (EM), and X-ray absorption near-edge spectroscopy (XANES) were used to observe multiscale structural changes to the air electrode, which are associated with degradation in cell performance. A combined EM-X-ray characterization approach was used to derive hierarchical changes to the crystal structure, microstructure, and elemental compositions. Atomistic modeling was performed to complement the experimental analyses and to understand thermodynamic stability ranges. This work provides an understanding of how LSCF degradation progresses, which informs mitigation strategies.

EXPERIMENTAL METHODS

The two electrolyte-supported button cells characterized in this study were from the same fabrication batch. The cell (Figure 1) is 3 cm in diameter and comprised of: a 10−20 µm air electrode consisting of a 6428-LSCF and GDC composite at a 1:1 ratio, a 5−8 µm GDC barrier layer, a 5−8 µm YSZ electrolyte, a 15−25 µm Ni-8YSZ (8 mol % Y_2O_3) fuel electrode functional layer, and a 400−500 µm Ni-3YSZ (3 mol % Y_2O_3) support layer. During fabrication, the YSZ electrolyte, Ni-YSZ fuel electrode, and Ni-YSZ support layer are cofired at 1350 °C. The GDC barrier layer is then screen printed onto the cell, which is sintered at 1230 °C before the LSCF/GDC composite is added and sintered at 1000 °C. Cells were contacted with Ag mesh and paste on the LSCF/GDC layer and with Ni paste and Pt wires on the Ni-YSZ support. Glass seals were used to secure the cell on an alumina support tube for testing. The cells prepared for testing were exposed to a Ni reduction process at 750 °C for 2 h in a 5% H_2, 95% N_2 atmosphere, before increasing the H_2 concentration to 100%. Cell open circuit voltage (OCV) was monitored to ensure that NiO was fully reduced to Ni. After reduction, humidity was introduced to the hydrogen stream through a heated bubbler held at 78 °C to achieve a gas composition of 50% H_2 and 50% H_2O (corrected for the elevation of the testing lab). The cells chosen for characterization include: an as-fabricated cell not yet sealed or contacted with current collectors and a cell tested for 1000 h at 750 °C, 1.3 V, and 50/50 H_2O/H_2 ratio.

Electrochemical testing was performed with a Solartron Analytical CellTest system consisting of a 1470E potentiostat with 1455A Series frequency response analyzers. Cells were tested potentiostatically at 1.3 V. Every 50 h, the potentiostatic hold was interrupted to measure the OCV for 1 min and collect an electrochemical impedance spectrum (EIS). EIS was performed with a DC offset of 1.3 V and an AC amplitude of 10 mV in the frequency range of 10 kHz to 0.1 Hz.

X-Ray Diffraction

XRD measurements were obtained at the Stanford Synchrotron Radiation Lightsource (SSRL), beamline 2-1, using an incident energy of 17 keV (0.729 Å). Angle-dispersive 2D diffraction data were acquired stepwise using a Pilatus 100K hybrid photon counting detector. The 2D images were subsequently normalized to the incident beam, stitched, and integrated using a Python script written specifically for SSRL beamline 2-1. Measurements were performed in a flat plate geometry with the air electrode facing upward, wherein the angle incident to the sample was controlled to attenuate the signal from buried SOEC layers. All data were obtained up to tth = 95° ($q \sim 12.7$ Å^{-1}). XRD data used to analyze crystalline structural changes were acquired with a 5° incident angle.

X-Ray Absorption Near-Edge Spectroscopy (XANES) and Micro X-ray Fluorescence (μ-XRF)

SOEC cells were mechanically fractured to expose the layers in the cross-section for characterization. Samples were mounted with the cell cross-section perpendicular to the path of the beam, with the surface of the cell cross-section mechanically polished to ensure uniformity of the sample. XANES measurements were obtained at SSRL beamline 2-3 using variable incident energies in fluorescence mode. The Fe K-edge was measured over a range of 6.882−7.227 keV by using an ∼5 × 5 μm^2 X-ray spot. The pre-edge region (6.882−7.092 keV) used an energy step size of 10 eV; the edge region (7.092−7.142 keV) used an energy step size of 0.35 eV; and the postedge region (7.142−7.227 keV) used an energy step of 0.66 eV. A Fe-foil reference was collected simultaneously. Spectra were collected in triplicate consecutively, and then averaged, background-subtracted, energy aligned via the Fe-foil reference, and normalized in Sixpack.[45] Corroborative μ-XRF elemental mapping was performed at an incident energy of 18.1 keV using an ∼1 × 1 μm^2 X-ray spot, a 1 μm step size, and a 50 ms dwell time. Data processing of the μ-XRF maps was performed in SMAK.[46]

SEM and TEM

The fractured portion of the cell was polished in cross-section using SiC grinding paper to prepare the surface for electron microscopy. SEM comparison of all cell components of regions with and without polishing confirms that this method of sample preparation does not alter the cell or cause artificial changes in the results. SEM-EDS on regions were collected using a TESCAN S8252G SEM/FIB to observe the cell structure in cross-section. SEM and EDS are useful in confirming that the trends found in TEM are representative of the bulk sample and also in locating areas of interest for TEM investigations.

Focused ion beam (FIB, FEI Co. Helios 600i) was used to prepare TEM specimens by using standard preparation methods. FIB allows TEM specimens to be specifically prepared from the relevant electrodes and interfaces. An example of these locations in the cell can be seen in Figure S1. STEM analyses were conducted on an FEI Co. Talos 200FX operated at 200 keV. EDS spectral images were collected on the same instrument and analyzed using Bruker Esprit v.2.9. STEM EDS maps were quantified using the Cliff−Lorimer techniques in ESPRIT Quantax software implementation (Bruker Nano Analytics, Berlin,Germany).

Modeling

Atomistic modeling was used to predict the thermodynamic stability of LSCF. We considered a collection of relevant phases, including a range of LSCF compositions in the ABO_3 perovskite and A_2BO_4 Ruddlesden−Popper (RP) structures, Co−Fe spinels (Co_3O_4, Fe_3O_4, and $CoFe_2O_4$), La_2O_3, SrO, and pure elements. To model the chemical disorder in LSCF phases, special quasirandom structures (SQSs) were generated using the Alloy Theoretic Automated Toolkit (ATAT).[47−51] SQSs of 80 atoms (16 formula units) and 56 atoms (8 formula units) were used for the ABO_3 and A_2BO_4 structures, respectively.

Total energies were calculated from density functional theory using the Vienna Ab initio Simulation Package (VASP).[52−55] Projector augmented-wave (PAW) pseudopotentials[56−58] were used, with the O 2s^2 2p^4, La 5s^2 5p^6 5d^1 6s^2, Sr 4s^2 4p^6 5s^2, Co 3d^7 4s^2, and Fe 3d^6 4s^2 states treated as valence states. A plane-wave energy cutoff of 520 eV was used. Brillouin zones were sampled with Γ-centered Monkhorst−Pack[59] k-point meshes of density 30 Å along each reciprocal lattice vector. The PBE exchange-correlation functional[60] was used along with Hubbard U corrections for Co and Fe applied using the approach of Dudarev.[61] U values of 3.4 and 4.0 eV were applied to the d electrons of Co and Fe, respectively, based on established calibrations to experimental formation enthalpies.[62] All calculations were spin-polarized, with magnetic moments initialized ferromagnetically except in the case of the Co−Fe spinels, where various nonferromagnetic orderings were considered. The atomic positions, cell shape, and volume of structures were fully relaxed prior to performing a final static calculation, except in the case of the LSCF SQS where only the volume and positions were relaxed. For the LSCF SQS structures, the Co charge and spin states were found to be highly sensitive to the initial volume, making it difficult to determine the equilibrium volume and energy. To address this, we performed a set of relaxations for each SQS structure using various initial magnetic moments for all Co ions (ranging from 0.6 μ_B to 5.0 μ_B) and selected the lowest resulting energy to represent each structure.

The energy of the O_2 molecule and the PBE+U energies of Co/Fe-containing oxide phases were adjusted based on well-established empirical corrections for oxide formation enthalpies.[62,63] In determining phase stability among the various structures, we assume that the system is open to oxygen at a chemical potential set by that of O_2 gas at temperature T and partial pressure p_{O_2}, given by

$$\mu_{O_2}(T, p_{O_2}) = E_{O_2} + \Delta\mu_{O_2}(T, p_{O_2})$$

$$\Delta\mu_{O_2}(T, p_{O_2}) = H^\circ_{O_2}(T) - TS^\circ_{O_2}(T) + k_B T \ln\left(\frac{p_{O_2}}{p^\circ}\right) \quad (1)$$

where E_{O_2} is the calculated energy of an O_2 molecule at 0 K and $H^\circ_{O_2}$ and $S^\circ_{O_2}$ are the enthalpy (relative to T = 0 K) and entropy, respectively, at $p_{O_2} = p^\circ = 0.1$ MPa, obtained from tabulated values.[64] Since the corrections employed for the DFT energies were calibrated to experimental reaction enthalpies at standard conditions, we also subtracted $H^\circ_{O_2}(T^\circ = 298.15\ \text{K})$ from the adjusted O_2 energy to obtain E_{O_2}. After choosing a particular value of μ_{O_2}, we construct the grand potential phase diagram[65] by finding the convex hull of equilibrium phases (with respect to the oxygen grand potential) and projecting its facets into the subspace of valid ABO_3 perovskite LSCF compositions (defined by having an A:B ratio of 1).

RESULTS AND DISCUSSION

Electrochemical Performance

The electrochemical performance of the 1000 h SOEC test is shown in Figure S2. The data show an initial activation period, with increasing current density over the first 35 h, which peaked at 1.22 A cm^{-2}. After the initial activation, the cell shows steady degradation, decreasing to 0.64 A cm^{-2} over the 1000 h test. Figure S3 shows the impedance spectra at 1.3 V every 50 h throughout the test. The initial activation can be seen as a decrease in the polarization resistance and total area-specific resistance over the first 50 h. Afterward, both the ohmic and polarization resistance increase throughout the test,

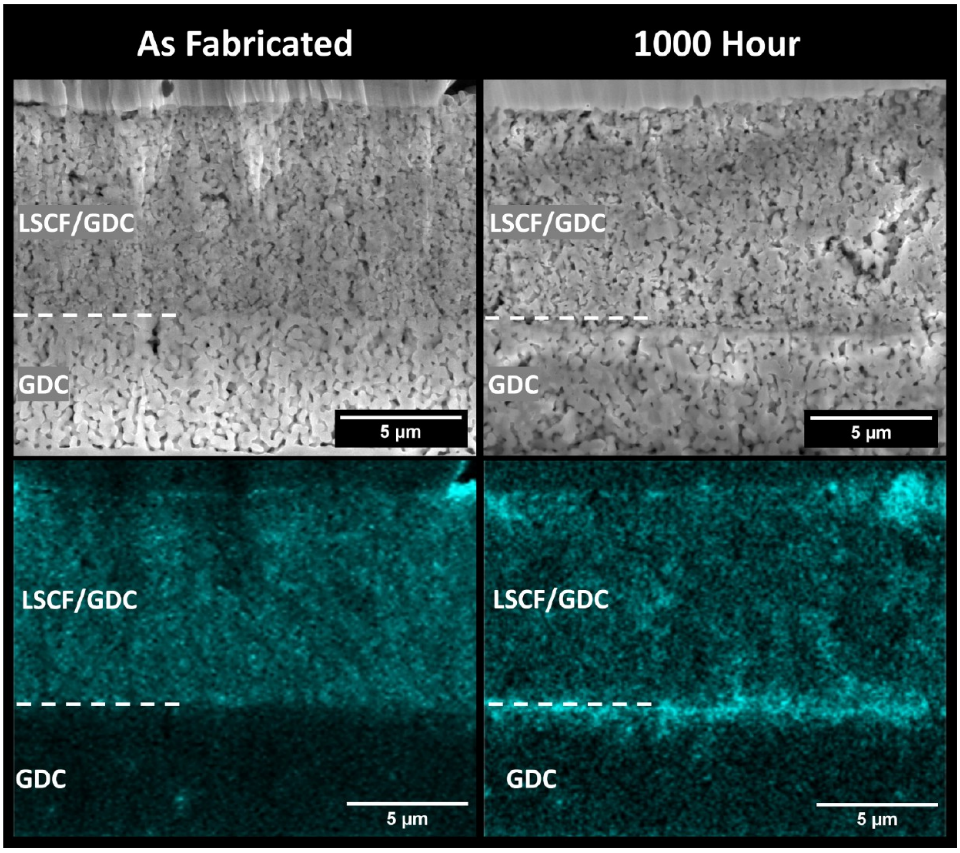

Figure 2. SEM imaging (top) and Sr Kα SEM-EDS spectral imaging (bottom) of the as fabricated cell (left) and 1000 h cell (right). The air electrode/GDC barrier layer interface is marked with a dashed line.

with the increase in polarization resistance contributing more to the overall degradation.

SEM-EDS

SEM on both as-fabricated and 1000 h SOECs indicates no mechanical delamination or large void formation occurred during cell fabrication, preparation, or testing. EDS mapping reveals Sr clustering and transport across much of the cell, as seen in Figure 2. Changes in Sr distribution are not clearly evident in the as-fabricated cell, whereas SEM-EDS of the 1000 h sample reveals Sr diffusion from within the LSCF/GDC air electrode to both the Ag boundary and the GDC boundary, indicating transport is not initially restricted to the direction of gas or current flow. This results in Sr clusters at the air electrode/barrier layer interface and migration through the barrier layer as the SOEC is operated for 1000 h. While the SEM-EDS results demonstrate the larger scale changes to the SOECs (10s-100s of micron scale), combined analyses from STEM-EDS, XRD, and XANES depict early onset LSCF decomposition and cation migration at smaller length scales (e.g., nano- to micrometers).

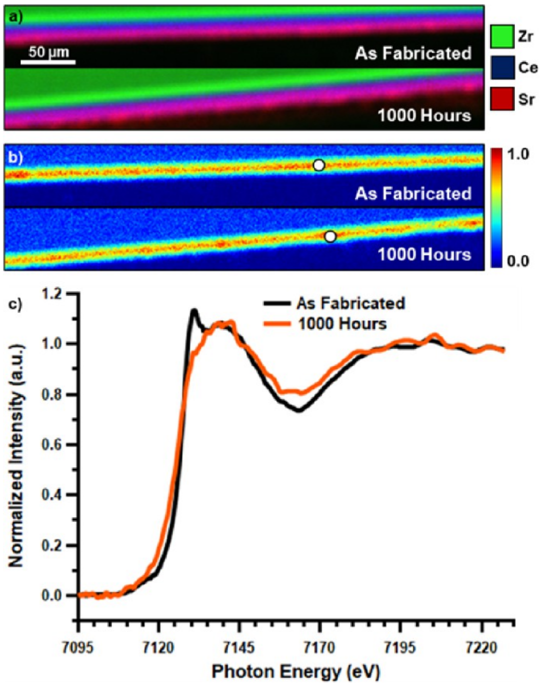

Figure 3. (a) μ-XRF tricolor map comparison of Zr, Ce, and Sr distribution, (b) Fe μ-XRF signal scaled from 0.0 to 1.0 with white circles added to show XANES measurement areas, and (c) Fe K-edge XANES spectra for the as fabricated and 1000 h samples.

μ-XRF and XANES

Elemental mapping by μ-XRF was performed to complement SEM-EDS, particularly for higher Z elements where μ-XRF has enhanced sensitivity relative to SEM-EDS. Tricolor maps showing Zr, Ce, and Sr distributions across cross-sections of the as-fabricated and 1000 h aged samples are displayed in Figure 3a. With a pixel size of 1 μm and a measurement area of $\sim 300 \times 50\ \mu m^2$, this technique does not identify any regions of Sr migration through the barrier layer, confirming no Sr secondary phases have formed that are larger than micron scale. This corroborates the SEM-EDS of both samples shown

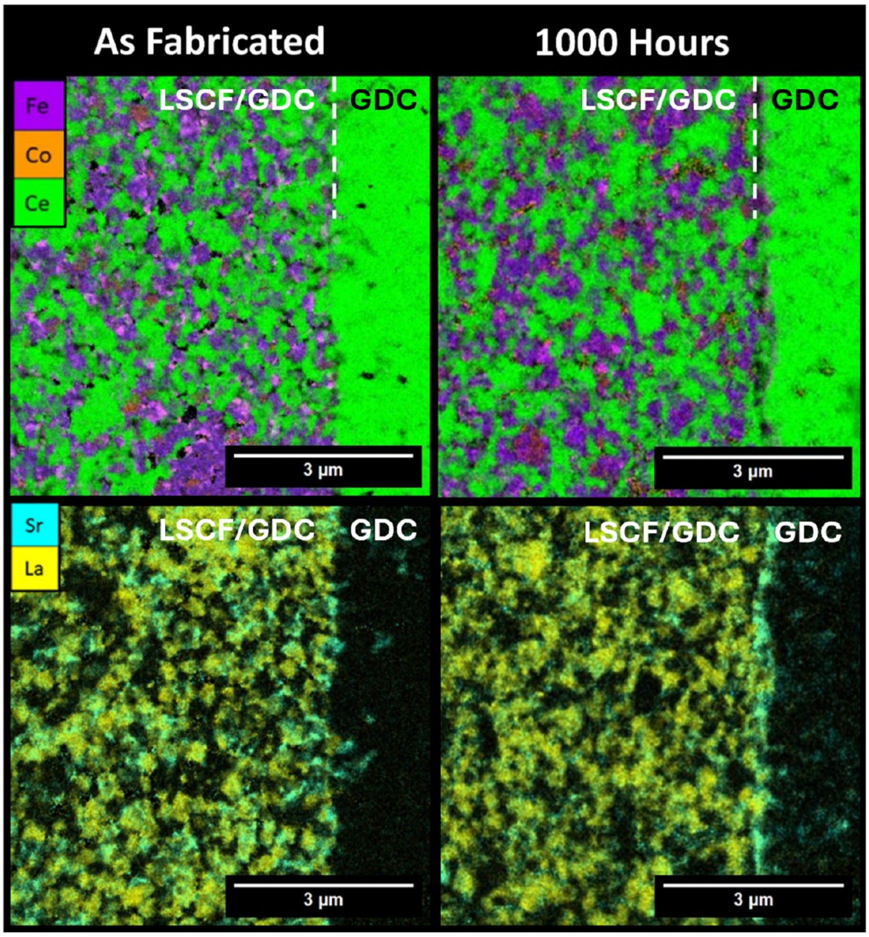

Figure 4. STEM-EDS maps overlaying (top) Fe, Co, and Ce and (bottom) Sr and La signals of the LSCF-GDC interface marked with dashed line.

in Figure 2, where Sr clusters within the barrier layer are well below the micron scale.

Fe-specific μ-XRF maps are displayed in Figure 3b, which also show little difference at the micron scale. Fe K-edge XANES spectra were obtained on ∼5 μm spots, which are highlighted in the XRF maps of both the as-fabricated and 1000 h aged samples (Figure 3b,c). Comparison of the two XANES spectra shows a clear negative shift between the as-fabricated and 1000 h samples, indicating that a degree of net reduction of Fe has occurred. This is confirmed by estimating edge step energy values (E_0) from the maximum value of the first derivative; the 1000 h sample has an E_0 of 7126.3 eV, 1.8 eV lower than that of the as-fabricated sample (Figure S4). This value of shift is somewhat larger in magnitude compared to a comparison of $SrFeO_3$ (Fe^{4+}) and $LaFeO_3$ (Fe^{3+}) from the literature, in which a 1.0 eV shift in E_0 was measured for reduction from Fe^{4+} to Fe^{3+}, and much smaller than the 3.5−4 eV shift from an Fe^{3+} to an Fe^{2+} state.[66] Within the expected 6428-LSCF structure, a net charge of +3.4 must be distributed across the B-site cations to satisfy charge neutrality when the oxygen vacancy concentration is very low. Locally, this can result in the presence of some Fe^{4+} and Co^{4+}. However, the presence of oxygen vacancies also affects the charge balance within the structure, complicating any attempt to estimate the exact expected Fe oxidation state.[13,26] A net reduction of Fe from the as-fabricated to 1000 h aged sample is consistent with either exsolution of Fe from 6428-LSCF as secondary phases with a lower net Fe oxidation statse (possible species include Fe_2O_3, Fe_3O_4, or various ternary Fe, Co spinel structures) are formed, or a decrease in the amount of the 6428-LSCF composition, as other stoichiometries with less Sr^{2+} content may require a lower average charge on the B-site. The magnitude of shift relative to the literature measurement of standards suggests the presence of some Fe^{2+} within the 1000 h sample; however, the complex nature of possible changes in Fe state within various LSCF stoichiometries and degrees of oxygen nonstoichiometry, and the possibility of the formation of secondary phases containing Fe^{2+}/Fe^{3+} prevent a conclusive identification of Fe-containing species from this analysis alone.

STEM-EDS

STEM-EDS spectral imaging of the as-fabricated sample reveals phase decomposition occurring in the LSCF during cell fabrication. With the intended 6428-LSCF composition, a stronger signal from Fe than Co is expected to appear purple in the EDS maps illustrated in Figure 4. Regions where Fe and Co are approximately equal or Co-dominated indicate phases that deviate from the intended composition, appearing as pink and orange, respectively, in Figure 4. STEM-EDS mapping of the as-fabricated sample primarily consists of LSCF with a stronger Fe signal (purple) and GDC (green), as is expected for 6428-LSCF. Additionally, regions of Co-rich and approximately equimolar Fe−Co are present. In the 1000 h cell, similar regions to those in the as-fabricated sample are indicative of secondary phase formation. La and Sr EDS maps are shown in Figure 4. Sr exsolution is apparent in both the as-fabricated and 1000 h cells, with an increase in the presence

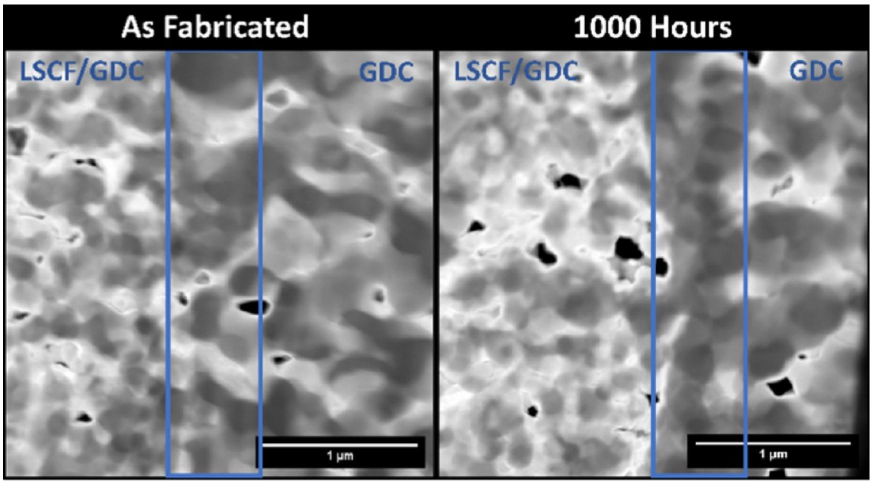

Figure 5. Dark field STEM with the air electrode/barrier layer interface marked with blue boxes.

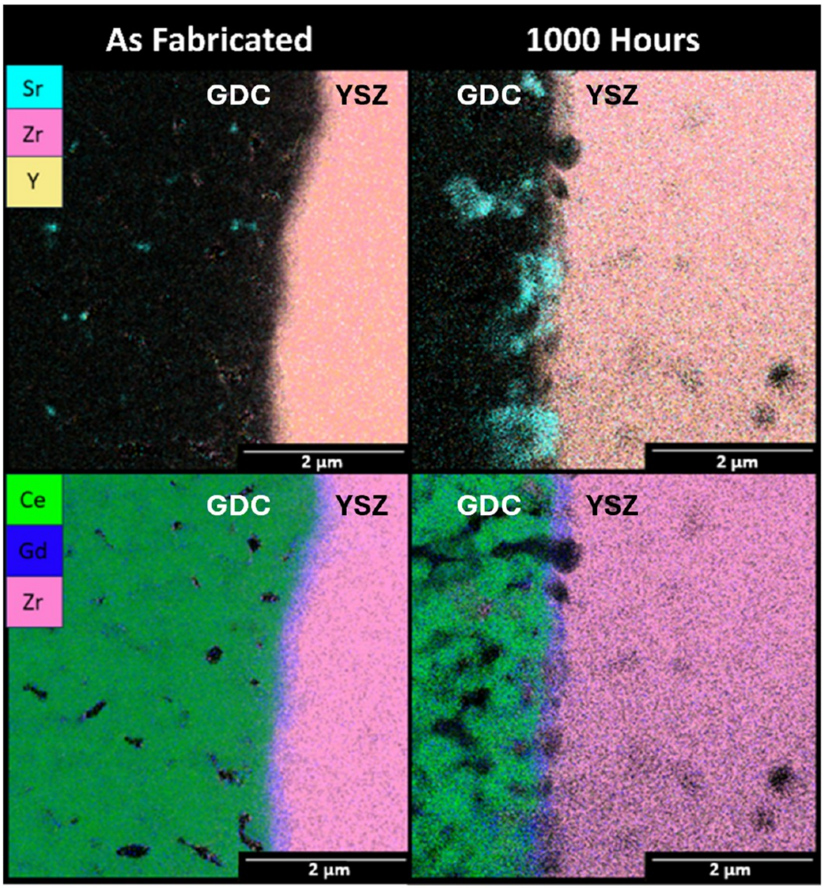

Figure 6. STEM-EDS mapping of the barrier layer/electrolyte interface, with Sr, Y, and Zr overlaid (top) and separately the Ce, Gd, and Zr signal overlaid (bottom).

and migration of secondary Sr-rich phases evident in the 1000 h cell. This can be observed in Figure 4 as Sr accumulates at the LSCF/GDC interface and migrates into the barrier layer.

Sr-rich phases accumulate at the air electrode/barrier layer interface, resulting in pore filling and densification at this interface, as seen in the dark field TEM images (Figure 5). Observing the interfaces from each sample, it is found that there is a notable increase in densification in the 1000 h cell in comparison to the as-fabricated baseline. It should be noted that while small amounts of air electrode degradation may lead to a small increase in density in the as-fabricated air electrode/barrier layer interface, the densification observed in the 1000 h cell is continuous at this interface in comparison. Electrode densification may slow gas transport and can also introduce thermo-mechanical strain to the system, leading to cracking and delamination.

STEM-EDS mapping of the GDC barrier layer and its interface with the YSZ electrolyte (Figure 6) in the as-fabricated sample indicates that a small amount of Sr is present in the barrier layer in the form of a pore-filling Sr phase in some of the open porosity. In this sample, the mobile Sr has not yet progressed to the barrier layer/electrolyte interface. In the 1000 h sample, the Sr found in the GDC barrier layer agglomerates to form particles from hundreds of nanometers to micrometer scale near the barrier layer/electrolyte interface to a much larger extent than in the as-fabricated cell. Sr-rich phases in the barrier layer fill the open porosity in the GDC and migrate through the barrier to the YSZ electrolyte. Sr migration to the YSZ interface in the 1000 h sample indicates a Sr−YSZ interaction, where clusters of Sr are seen infiltrating into the YSZ interface; this likely indicates the formation of $SrZrO_3$, which is further investigated with XRD. $SrZrO_3$ is potentially problematic as it exhibits reduced ionic conductivity relative to YSZ and GDC.[67] Additionally, thin continuous Gd and Ce layers are observed at the GDC/YSZ boundary (Figure 6). This feature is present in the as-fabricated sample and remains consistent after 1000 h of testing, so it is unlikely to be contributing to performance losses observed herein.

XRD

XRD results (Figure 7) of the as-fabricated and 1000 h samples are complex, indicating multiple phases present. If the air electrode contained only the intended 6428-LSCF and GDC, XRD should find only two distinct phases: rhombohedral LSCF (r-LSCF) (ICSD 186173) and fluorite-structured GDC (ICSD 259969). As cation composition varies in LSCF, structural changes occur, and multiple LSCF phases should be considered when analyzing XRD data. Rhombohedral LSCF occurs for La-/Fe-rich compositions, which include the targeted 6428-LSCF. As compositions shift to La-/Co- rich LSCF, a phase transformation to orthorhombic LSCF (o-LSCF) takes place. When Sr-/Fe- rich, LSCF adopts a cubic structure (ICSD 158799). Minute quantities of c-LSCF and o-LSCF are observed in the as-fabricated cell XRD results (Figure 7a) confirming compositional changes in the 6428-LSCF occur before the SOEC is mounted on the test stack, indicating degradation in the air electrode occurs during cell fabrication.

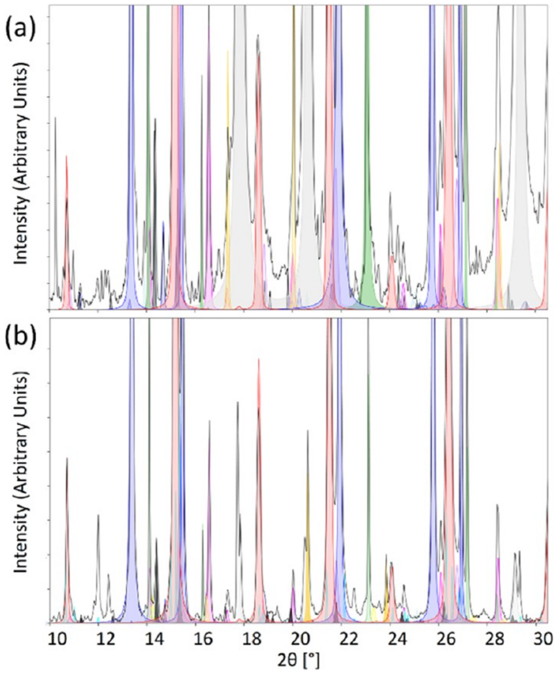

Figure 7. X-ray diffraction from the (a) before reduction and (b) 1000 h-aged samples. The expected phases are LSCF ($R\overline{3}c$) (red), GDC (blue), YSZ (green), Ni/NiO (orange), and the Ag (ICSD 22434) contact (gray). Secondary phases observed are $Co_{1-x}Fe2+_xO_4$ (magenta), LSCF (*Pnma*) (cyan), LSCF (*Pm*-3m) (lavender), LSCF (*I*4/*mmm*) (black), $SrZrO_3$ (light blue), and SrO (yellow).

The predominant phases identified in Figure 7 are r-LSCF and fluorite GDC phases intended in the SOEC (6428-LSCF and GDC), as well as the expected YSZ and NiO (ICSD 75316, ICSD 8688) phases (as-fabricated only). Further analysis of the XRD data also uncovered the presence of secondary phase formation, most notably including a range of cobalt ferrite spinel (AB_2O_4) structures (where A is Co^{2+}/Fe^{2+}) (examples of this range include Fe_3O_4: ICSD 183969, $Co_{0.15}Fe_{2.85}O_4$: ICSD 29894, $CoFe_2O_4$: ICSD 230939, $Co_{2.452}Fe_{0.34}O_4$: ICSD 12814, and Co_3O_4: ICSD 32839), indicating that a portion of the initial 6428-LSCF is present in a Co/Fe-deficient state. Most cobalt ferrite spinels (normal, inverse, and mixed) are composed of $2^+/3^+$ oxidation states, which reinforces the Fe K-edge XANES data shown in Figure 2 and alludes to a mechanism of phase segregation shown in Figure 4. While there are various ways LSCF can phase segregate, the most plausible explanation for the as-fabricated sample is equimolar loss of Sr and Co/Fe from the ABO_3 LSCF perovskite, given the uncorrelated Sr migration from STEM-EDS and cobalt ferrite spinel from XRD. Any unbalanced segregation of cations from the A or B sites of LSCF would cause a structural transformation to a series of off-stoichiometric phases where $A \neq B$, which were not identified in XRD from the as-fabricated sample. Although no SrO is detected, the domain sizes may be too small and limit coherence, making it challenging, if not impossible, to detect with synchrotron XRD despite the substantial signal-to-noise ratio and resolution.

Additionally, the shouldering of the observed 6428-LSCF peaks (e.g., (2−10) and (−114) reflections combined at 15.2°) indicates that a small amount of *o*-LSCF is present. Despite the structural similarity between the two structures, the symmetry differences of *r*-LSCF and *o*-LSCF induce additional Bragg reflections (e.g., 210, 031, and 212) for *o*-LSCF that can be differentiated from *r*-LSCF and *c*-LSCF. Subsequent XRD measurements with a high-resolution Si analyzer crystal later confirmed that the observed shouldering of *r*-LSCF peaks was sample-induced rather than an instrumental contribution.

In agreement with STEM-EDS, XRD of the 1000 h sample indicates that structural changes to the LSCF progress with cell operation. Similar to the as-fabricated XRD data, the 1000 h XRD showed both expected phases from fabrication as well as new secondary phases resulting from cell operation. While the secondary phases are qualitatively identified, their relative weight percentages are too small to be reliably included in quantitative phase analyses derived from Rietveld refinements (see Figure S5). These new secondary phases comprise tetragonal, RP LSCF (A_2BO_4, $A_4B_3O_{10}$), a Sr-deficient rhombohedral LSCF, a Sr-rich cubic LSCF, and cubic $SrZrO_3$. The diffraction patterns from these structures, in addition to a few unidentified structures, are displayed in Figure 7b. The 1000 h sample definitively confirms the presence of SrO and $SrZrO_3$ validating the STEM-EDS results indicating that exsolved Sr migrated to the YSZ and subsequently reacted with the zirconate present at the interface and within the YSZ.

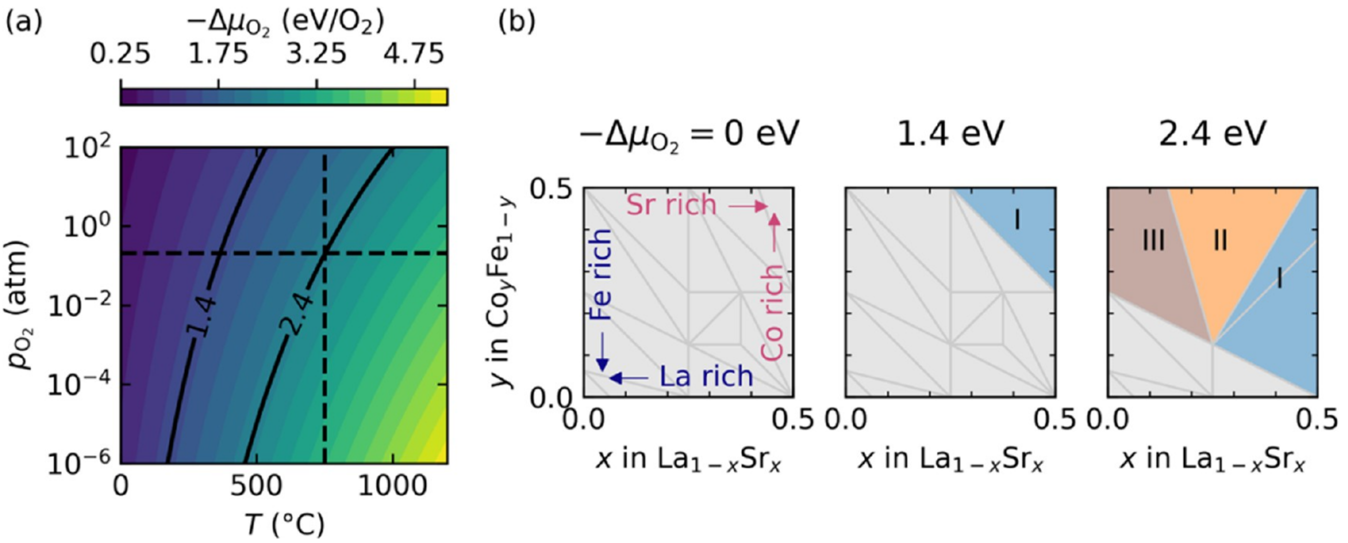

Figure 8. (a) Oxygen chemical potential (vs O_2 at 0 K, plotted as a negative) as a function of the temperature and partial pressure. Solid contours indicate chemical potential values used in (b) and dotted lines indicate 750 °C and 0.21 atm O_2. (b) Phase stability maps of perovskite LSCF at different values of the oxygen chemical potential. Light gray regions indicate stability of perovskite LSCF and colored/numbered regions indicate formation of secondary phases (described in the text and detailed in Figure S8).

Combined results from electron microscopy and X-ray characterization are self-consistent and elucidate the structural and compositional changes to 6428-LSCF during SOEC preparation and HTE operation. The results indicate equimolar loss of Sr and Co/Fe with subsequent migration and cobalt ferrite spinel formation, resulting in unintended LSCF compositions. Secondary and off-stoichiometry LSCF phases are present in the as-fabricated cell and are increased in the cell tested for 1000 h, indicating LSCF initial degradation occurs during cell processing (likely at the high-temperature sintering steps) and proceeds with cell testing. The identified secondary phases have reduced conductivity relative to LSCF, and cation migration to the air electrode/barrier layer interface results in densification at that interface, which will likely have implications for the mechanical integrity of the cell.

Thermodynamic Modeling

Thermodynamic modeling based on density functional theory calculations was performed to examine the stability of the LSCF and explain the cause of structural and compositional changes observed with electron microscopy and X-ray characterization techniques discussed previously. Although kinetic effects likely play an important role, thermodynamics provides a starting point for studying possible mechanisms of LSCF decomposition. We note that the stability of LSCF has previously been investigated using the CALPHAD approach,[68−70] which is typically informed by experimental measurements. However, this method can exhibit reduced accuracy when extrapolating data to higher-order multicomponent systems. Furthermore, a fundamental understanding of LSCF thermodynamics from first-principles calculations has yet to be established. *r*-LSCF was the primary focus of the atomistic modeling, as it is the predominant structure observed experimentally in this study. As shown in Figure S6, *r*-LSCF becomes inherently less stable (with respect to the pure elements) with increasing Sr and Co content. A similar trend is seen for LSCF in the tetragonal A_2BO_4 RP structure (Figure S7). To predict secondary phase formation, we consider the relative stability of perovskite LSCF versus other polymorphs and compositions as a function of thermodynamic and environmental conditions described via oxygen chemical potential μ_{O_2}. Following eq 1, μ_{O_2} depends on temperature and O_2 partial pressure p_{O_2}, with higher T and lower p_{O_2} resulting in lower μ_{O_2} (Figure 8a). This could in turn promote the formation of less oxygen-rich oxide phases (e.g., spinel) from perovskite LSCF.

Figure 8b shows predicted stability maps of LSCF with varying μ_{O_2}. Light gray regions indicate that perovskite LSCF remains stable, while the colored regions indicate partial decomposition into the following phases:

I. (blue): Co_3O_4 spinel and Sr-rich RP phase
II. (orange): Co_3O_4 spinel, Sr-rich RP phase, and La_2O_3
III. (brown): Co_3O_4 spinel and La_2O_3

(see Figure S8 for the specific phases predicted in each case). The secondary phases begin to appear at higher Sr/Co concentrations, before spreading to lower ones with decreasing μ_{O_2}, while perovskite LSCF remains stable in the La-/Fe-rich corner, at least for the values of μ_{O_2} shown in Figure 8b. The trend of decreasing stability with increasing Sr/Co content is consistent with findings from previous CALPHAD work.[68] Note that we have modeled each phase here as a line compound, even though the true LSCF phases (perovskite and RP) likely behave as solid solutions. Thus, the predicted regions of coexistence between different LSCF phases (e.g., the gray triangular facets in Figure 8b) may be better understood as proxies for solid solution regions. The exception would be a scenario in which the coexistence of two perovskite LSCF phases with different structures (e.g., rhombohedral and orthorhombic) at different compositions is preferred over a single LSCF solid solution phase. This type of scenario is consistent with our observation of multiple perovskite LSCF phases (Sr-deficient rhombohedral and Sr-rich cubic) in the 1000 h sample.

Focusing on the intended 6428-LSCF composition, we can track the extent of secondary phase formation across conditions. Figure 9a shows the predicted mole fractions of

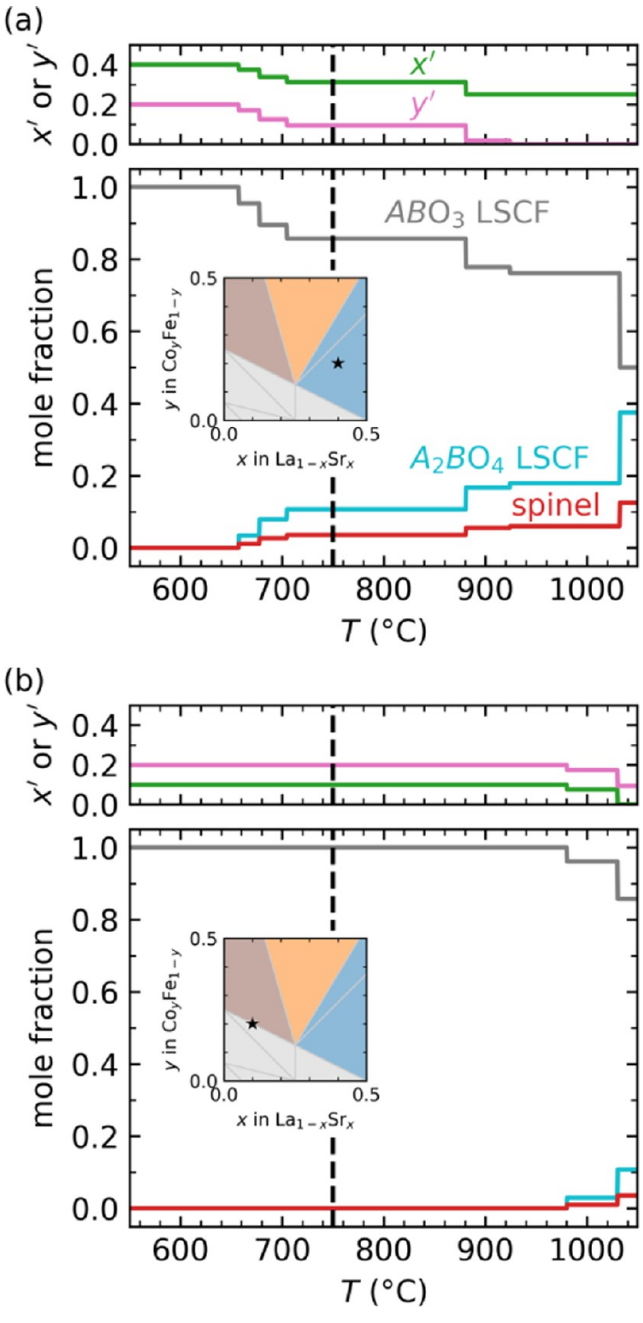

Figure 9. Predicted mole fractions of different phases (grouped by crystal structure) vs temperature at 0.21 atm O_2 and an overall composition of (a) 6428-LSCF and (b) 9128-LSCF. Insets show the predicted phase diagram at 750 °C and 0.21 atm O_2, with the overall composition marked by a star. Dotted lines indicate this temperature. The upper panels in panels a and (b) track the Sr content x and the Co content y of the remaining ABO_3 LSCF.

each phase (grouped by structure) versus temperature at 0.21 atm of O_2, the partial pressure of O_2 in air. The onset of 6428-LSCF decomposition in this case occurs around 650 °C with the formation of tetragonal (RP A_2BO_4) LSCF and Co_3O_4 spinel, and the fractions of these phases grow with increasing temperature. The remaining perovskite LSCF becomes increasingly Co- and Sr-deficient, as shown in the top panel of Figure 9a. In contrast, La- and Fe-rich compositions remain stable at much higher temperatures. For example, Figure 9b shows that 9128-LSCF is not predicted to decompose in air until around 1000 °C. While this is well above the temperature of typical SOEC operation, it is common for sintering temperatures that LSCF may experience during fabrication or processing steps such as sealing or contacting to reach or exceed 1000 °C (recall the sintering temperatures used in fabricating the current SOECs is 1000 °C). Figure 9 suggests, however, that 6428-LSCF will display significantly greater decomposition in this temperature regime.

Varying O_2 partial pressure has the opposite effect of varying temperature on stability (Figure S9). Thus, if lower p_{O_2} conditions are encountered during SOEC processing or operation (especially locally), the onset of decomposition would shift to lower temperatures. Truly quantitative predictions of LSCF degradation will rely on precise knowledge of local temperature and pressure conditions at the air electrode, as well as further refinements to our thermodynamic model, such as accounting for configurational entropy and oxygen nonstoichiometry of the solid phases. These refinements, as well as kinetic effects, may explain discrepancies between our predictions and experimental observations, such as the formation of mixed Co−Fe spinels, and will be detailed in future computational studies.

■ CONCLUSION

Decomposition of the air electrode and secondary phase formation in SOECs impact cell performance. Understanding the onset of material decomposition, including the underlying causes, is critical to developing mitigation strategies. Avoiding/diminishing early onset degradation may slow performance loss or prevent catastrophic failure later in cell life after tens of thousands of hours of operation.

In the present study, we used a multifaceted characterization approach to evaluate a cell as fabricated and a cell that had been tested for 1000 h, each with the commonly used 6428-LSCF as the mixed ionic/electronic conducting phase in the air electrode. 6428-LSCF degraded into unintended LSCF phases during fabrication, likely due to sintering at 1000 °C, and continued during testing at 750 °C, in alignment with thermodynamic modeling results demonstrating that 6428-LSCF is not stable under these conditions. Decomposition of 6428-LSCF progresses during testing, resulting in increased secondary phase formation and migration of Sr into and through the GDC barrier layer, forming a dense layer at the electrode/barrier layer interface and $SrZrO_3$ at the barrier layer/electrolyte interface. These results are concerning as unintended LSCF phases lack the conductivity of 6428, $SrZrO_3$ is a known ionic insulator. Furthermore, secondary phase accumulation at interfaces may increase resistance, and densification may alter the mechanical integrity of the cell, increasing the risk of eventual cracking and delamination.

Modeling suggests that LSCF-6428 might be stable if it does not exceed 650 °C, but that is not currently compatible with common manufacturing processes and cell materials (sealants and contacts) and may result in insufficient sintering and thus inadequate mechanical properties. Modeling efforts identify 9128-LSCF as a more stable alternative LSCF composition with a decomposition onset temperature predicted above 950 °C. While literature demonstrates that 9128-LSCF is ∼5× less conductive (total conductivity) than 6428-LSCF,[13] it is unclear if the difference in initial SOEC performance that may result from this conductivity difference will outweigh the potential benefit to lifetime hydrogen production possible if the LSCF decomposition process is avoided/slowed. This work suggests that further investigation, including experimental, atomistic modeling, and cell/system modeling, is needed to evaluate the holistic impact of using other stoichiometries of LSCF that avoid such early onset cell degradation as observed in this study.

■ ASSOCIATED CONTENT

Supporting Information

The Supporting Information is available free of charge at https://pubs.acs.org/doi/10.1021/acsphyschemau.4c00095.

> SEM of the location of TEM lamella to capture all active layers, electrochemical testing results of tested cell, first derivative of Fe K-edge XANES spectra, Rietveld refinement figures used in XRD, calculated formation energies (vs pure elements) of ABO_3 and A_2BO_4 LSCF, and additional computational details including phase stability maps at varying oxygen chemical potential, predicted secondary phase fractions vs temperature and oxygen partial pressure at an overall composition of 6428-LSCF (PDF)

■ AUTHOR INFORMATION

Corresponding Authors

Kyoung E. Kweon − *Lawrence Livermore National Laboratory, Livermore, California 94550, United States;* orcid.org/0000-0001-5155-3789; Email: kweon1@llnl.gov

Brian P. Gorman − *Colorado School of Mines, Golden, Colorado 80401, United States*; Email: bgorman@mines.edu

Sarah Shulda − *National Renewable Energy Laboratory, Golden, Colorado 80401, United States;* Email: sarah.shulda@nrel.gov

Authors

Heather S. Slomski − *Colorado School of Mines, Golden, Colorado 80401, United States; National Renewable Energy Laboratory, Golden, Colorado 80401, United States;* orcid.org/0000-0001-5255-3481

Jonas L. Kaufman − *Lawrence Livermore National Laboratory, Livermore, California 94550, United States;* orcid.org/0000-0002-0814-9462

Michael J. Dzara − *National Renewable Energy Laboratory, Golden, Colorado 80401, United States;* orcid.org/0000-0001-8125-0586

Nicholas A. Strange − *Stanford Synchrotron Radiation Lightsource, SLAC National Accelerator Laboratory, Menlo Park, California 94025, United States;* orcid.org/0000-0001-5699-7274

Cameron Priest − *Idaho National Laboratory, Idaho Falls, Idaho 83415, United States*

Jeremy L. Hartvigsen − *Idaho National Laboratory, Idaho Falls, Idaho 83415, United States*

Nicholas Kane − *Idaho National Laboratory, Idaho Falls, Idaho 83415, United States*

Micah Casteel − *Idaho National Laboratory, Idaho Falls, Idaho 83415, United States*

Brandon C. Wood − *Lawrence Livermore National Laboratory, Livermore, California 94550, United States*

David S. Ginley − *National Renewable Energy Laboratory, Golden, Colorado 80401, United States*

Complete contact information is available at: https://pubs.acs.org/10.1021/acsphyschemau.4c00095

Notes

The authors declare no competing financial interest.

■ ACKNOWLEDGMENTS

This work was authored in part by the National Renewable Energy Laboratory, operated by Alliance for Sustainable Energy, LLC, for the U.S. Department of Energy (DOE) under Contract No. DE-AC36-08GO28308. The work authored by Idaho National Laboratory was performed under Contract No. DE-AC07-05ID14517 with the U.S. Department of Energy. The work authored by Lawrence Livermore National Laboratory was performed under the auspices of the U.S. Department of Energy (DOE) under Contract No. DE-AC52-07NA27344. Funding was provided by the U.S. Department of Energy Office of Energy Efficiency and Renewable Energy Hydrogen Fuel Technology Office through the H2NEW consortium. The views expressed in the article do not necessarily represent the views of the DOE or the U.S. Government. The U.S. Government retains, and the publisher, by accepting the article for publication, acknowledges that the U.S. Government retains a nonexclusive, paid-up, irrevocable, worldwide license to publish or reproduce the published form of this work, or allow others to do so, for U.S. Government purposes. Use of the Stanford Synchrotron Radiation Lightsource, SLAC National Accelerator Laboratory, is supported by the U.S. Department of Energy, Office of Science, Office of Basic Energy Sciences under Contract No. DE-AC02-76SF00515. Use of computational resources is sponsored by the DOE's EERE and located at the National Renewable Energy Laboratory.

■ REFERENCES

(1) Laguna-Bercero, M. A. Recent Advances in High Temperature Electrolysis Using Solid Oxide Fuel Cells: A Review. *J. Power Sources* **2012**, *203*, 4−16.

(2) Elder, R.; Cumming, D.; Mogensen, M. B. Chapter 11 - High Temperature Electrolysis. In *Carbon Dioxide Utilisation*, Styring, P.; Quadrelli, E. A.; Armstrong, K.; Elsevier: Amsterdam, 2015; pp. 183−209. .

(3) Ferrero, D.; Lanzini, A.; Santarelli, M.; Leone, P. A Comparative Assessment on Hydrogen Production from Low- and High-Temperature Electrolysis. *Int. J. Hydrogen Energy* **2013**, *38* (9), 3523−3536.

(4) Wang, F.; Wang, L.; Ou, Y.; Lei, X.; Yuan, J.; Liu, X.; Zhu, Y. Thermodynamic Analysis of Solid Oxide Electrolyzer Integration with Engine Waste Heat Recovery for Hydrogen Production. *Case Stud. Therm. Eng.* **2021**, *27*, 101240.

(5) Yilanci, A.; Dincer, I.; Ozturk, H. K. A Review on Solar-Hydrogen/Fuel Cell Hybrid Energy Systems for Stationary Applications. *Prog. Energy Combust. Sci.* **2009**, *35* (3), 231−244.

(6) Mohebali Nejadian, M.; Ahmadi, P.; Houshfar, E. Comparative Optimization Study of Three Novel Integrated Hydrogen Production Systems with SOEC, PEM, and Alkaline Electrolyzer. *Fuel* **2023**, *336*, 126835.

(7) Cao, Y.; Zoghi, M.; Habibi, H.; Raise, A. Waste Heat Recovery of a Combined Solid Oxide Fuel Cell - Gas Turbine System for Multi-Generation Purposes. *Appl. Therm. Eng.* **2021**, *198*, 117463.

(8) Wendt, D. S.; Knighton, L. T.; Boardman, R. D. *High Temperature Steam Electrolysis Process Performance and Cost Estimates; INL/RPT-22−66117-Rev000*; Idaho National Laboratory (INL), Idaho Falls, ID (United States), 2022. .

(9) Effori, E.; Laurencin, J.; Silva, E. D. R.; Hubert, M.; David, T.; Petitjean, M.; Geneste, G.; Dessemond, L.; Siebert, E. An Elementary

Kinetic Model for the LSCF and LSCF-CGO Electrodes of Solid Oxide Cells: Impact of Operating Conditions and Degradation on the Electrode Response. *J. Electrochem. Soc.* **2021**, *168* (4), 044520.

(10) Lu, Z.; Darvish, S.; Hardy, J.; Templeton, J.; Stevenson, J.; Zhong, Y. SrZrO3 Formation at the Interlayer/Electrolyte Interface during (La1-xSrx)1-δCo1-yFeyO3 Cathode Sintering. *J. Electrochem. Soc.* **2017**, *164* (10), F3097.

(11) Kim, S. J.; Choi, G. M. Stability of LSCF Electrode with GDC Interlayer in YSZ-Based Solid Oxide Electrolysis Cell. *Solid State Ionics* **2014**, *262*, 303−306.

(12) Monaco, F.; Ferreira-Sanchez, D.; Hubert, M.; Morel, B.; Montinaro, D.; Grolimund, D.; Laurencin, J. Oxygen Electrode Degradation in Solid Oxide Cells Operating in Electrolysis and Fuel Cell Modes: LSCF Destabilization and Interdiffusion at the Electrode/Electrolyte Interface. *Int. J. Hydrogen Energy* **2021**, *46* (62), 31533−31549.

(13) Tai, L.-W.; Nasrallah, M. M.; Anderson, H. U.; Sparlin, D. M.; Sehlin, S. R. Structure and Electrical Properties of La1 − xSrxCo1 − yFeyO3. Part 2. The System La1 − xSrxCo0.2Fe0.8O3. *Solid State Ionics* **1995**, *76* (3), 273−283.

(14) Pan, Z.; Liu, Q.; Lyu, R.; Li, P.; Chan, S. H. Effect of La0.6Sr0.4Co0.2Fe0.8O3−δ Air Electrode−Electrolyte Interface on the Short-Term Stability under High-Current Electrolysis in Solid Oxide Electrolyzer Cells. *J. Power Sources* **2018**, *378*, 571−578.

(15) Rashkeev, S. N.; Glazoff, M. V. Atomic-Scale Mechanisms of Oxygen Electrode Delamination in Solid Oxide Electrolyzer Cells. *Int. J. Hydrogen Energy* **2012**, *37* (2), 1280−1291.

(16) Khan, M. S.; Xu, X.; Knibbe, R.; Zhu, Z. Air Electrodes and Related Degradation Mechanisms in Solid Oxide Electrolysis and Reversible Solid Oxide Cells. *Renewable Sustainable Energy Rev.* **2021**, *143*, 110918.

(17) Jayapragasam, P.; Wen, Y.; Cook, K.; Wrubel, J. A.; Ma, Z.; Huang, K.; Jin, X. Crack Growth Rate at Oxygen Electrode/Electrolyte Interface in Solid Oxide Electrolysis Cells Predicted by Experiment Coupled Multiphysics Modeling. *J. Electrochem. Soc.* **2023**, *170* (5), 054509.

(18) Park, B.-K.; Zhang, Q.; Voorhees, P. W.; Barnett, S. A. Conditions for Stable Operation of Solid Oxide Electrolysis Cells: Oxygen Electrode Effects. *Energy Environ. Sci.* **2019**, *12* (10), 3053−3062.

(19) Chen, K.; Jiang, S. P. Surface Segregation in Solid Oxide Cell Oxygen Electrodes: Phenomena, Mitigation Strategies and Electrochemical Properties. *Electrochem. Energy Rev.* **2020**, *3* (4), 730−765.

(20) Porotnikova, N.; Osinkin, D. Segregation and Interdiffusion Processes in Perovskites: A Review of Recent Advances. *J. Mater. Chem. A* **2024**, *12* (5), 2620−2646.

(21) Nechache, A.; Hody, S. Alternative and Innovative Solid Oxide Electrolysis Cell Materials: A Short Review. *Renewable Sustainable Energy Rev.* **2021**, *149*, 111322.

(22) Lei, C.; Simpson, M. F.; Virkar, A. V. Investigation of Ion and Electron Conduction in the Mixed Ionic-Electronic Conductor- La-Sr-Co-Fe-Oxide (LSCF) Using Alternating Current (AC) and Direct Current (DC) Techniques. *J. Electrochem. Soc* **2022**, *169* (1), 014506.

(23) Niemczyk, A.; Świerczek, K. Development of Novel Air Electrode Materials for the SOFC and SOEC Technologies. *E3S Web Conf.* **2019**, *108*, 01019.

(24) Sadykov, V.; Kharlamova, T.; Batuev, L.; Muzykantov, V.; Mezentseva, N.; Krieger, T.; Alikina, G.; Lukashevich, A.; Rogov, V.; Zaikovskii, V.; Ishchenko, A.; Salanov, A.; Boronin, A.; Koscheev, S.; Pavlova, S.; Uvarov, N.; Smirnova, A.; Vasylyev, O. La0.8Sr0.2Ni0.4-Fe0.6O3−Ce0.8Gd0.2O2−δ Nanocomposite as Mixed Ionic−Electronic Conducting Material for SOFC Cathode and Oxygen Permeable Membranes: Synthesis and Properties. *Compos. Interfaces* **2009**, *16* (4−6), 407−431.

(25) Jiang, S. P. Development of Lanthanum Strontium Cobalt Ferrite Perovskite Electrodes of Solid Oxide Fuel Cells − A Review. *Int. J. Hydrogen Energy* **2019**, *44* (14), 7448−7493.

(26) Bouwmeester, H. J. M.; Den Otter, M. W.; Boukamp, B. A. Oxygen Transport in La0.6Sr0.4Co1−y Fe y O3−δ. *J. Solid State Electrochem.* **2004**, *8* (9), 599−605.

(27) Tietz, F.; Mai, A.; Stöver, D. From Powder Properties to Fuel Cell Performance − A Holistic Approach for SOFC Cathode Development. *Solid State Ionics* **2008**, *179* (27), 1509−1515.

(28) Tietz, F.; Haanappel, V. A. C.; Mai, A.; Mertens, J.; Stöver, D. Performance of LSCF Cathodes in Cell Tests. *J. Power Sources* **2006**, *156* (1), 20−22.

(29) Simner, S. P.; Anderson, M. D.; Engelhard, M. H.; Stevenson, J. W. Degradation Mechanisms of La − Sr − Co − Fe − O3 SOFC Cathodes. *Electrochem. Solid-State Lett.* **2006**, *9* (10), A478.

(30) Wang, H.; Yakal-Kremski, K. J.; Yeh, T.; Rupp, G. M.; Limbeck, A.; Fleig, J.; Barnett, S. A. Mechanisms of Performance Degradation of (La,Sr)(Co,Fe)O3-δ Solid Oxide Fuel Cell Cathodes. *J. Electrochem. Soc.* **2016**, *163* (6), F581.

(31) McPhail, S. J.; Frangini, S.; Laurencin, J.; Effori, E.; Abaza, A.; Padinjarethil, A. K.; Hagen, A.; Léon, A.; Brisse, A.; Vladikova, D.; Burdin, B.; Bianchi, F. R.; Bosio, B.; Piccardo, P.; Spotorno, R.; Uchida, H.; Polverino, P.; Adinolfi, E. A.; Postiglione, F.; Lee, J.-H.; Moussaoui, H.; Van Herle, J. Addressing Planar Solid Oxide Cell Degradation Mechanisms: A Critical Review of Selected Components. *Electrochem. Sci. Adv.* **2022**, *2* (5), No. e2100024.

(32) Hardy, J. S.; Coyle, C. A.; Bonnett, J. F.; Templeton, J. W.; Canfield, N. L.; Edwards, D. J.; Mahserejian, S. M.; Ge, L.; Ingram, B. J.; Stevenson, J. W. Evaluation of Cation Migration in Lanthanum Strontium Cobalt Ferrite Solid Oxide Fuel Cell Cathodes via In-Operando X-Ray Diffraction. *J. Mater. Chem. A* **2018**, *6* (4), 1787−1801.

(33) Shao, Q.; Jin, D.; Lu, Y.; Yu, Y.; Luo, L.; Sun, X.; Guan, C.; Wang, J.-Q. Performance Evolution Analysis of Solid Oxide Electrolysis Cells Operating at High Current Densities. *Int. J. Hydrogen Energy* **2024**, *57*, 709−716.

(34) Wang, Y.; Li, W.; Ma, L.; Li, W.; Liu, X. Degradation of Solid Oxide Electrolysis Cells: Phenomena, Mechanisms, and Emerging Mitigation Strategies—A Review. *J. Mater. Sci. Technol.* **2020**, *55*, 35−55.

(35) Crossley, K.; Montinaro, D. Insights into Strontium Zirconate-Induced Interface Pressures in Solid Oxide Electrolysis Cells. *J. Power Sources* **2024**, *589*, 233747.

(36) Bernadet, L.; Segura-Ruiz, J.; Yedra, L.; Estrade, S.; Peiró, F.; Montinaro, D.; Torrell, M.; Morata, A.; Tarancón, A. Enhanced Diffusion Barrier Layers for Avoiding Degradation in SOFCs Aged for 14000 h during 2 Years. *J. Power Sources* **2023**, *555*, 232400.

(37) Morales, M.; Miguel-Pérez, V.; Tarancón, A.; Slodczyk, A.; Torrell, M.; Ballesteros, B.; Ouweltjes, J. P.; Bassat, J. M.; Montinaro, D.; Morata, A. Multi-Scale Analysis of the Diffusion Barrier Layer of Gadolinia-Doped Ceria in a Solid Oxide Fuel Cell Operated in a Stack for 3000 h. *J. Power Sources* **2017**, *344*, 141−151.

(38) Gorman, B. P.; Anderson, H. U. Processing of Composite Thin Film Solid Oxide Fuel Cell Structures. *J. Am. Ceram. Soc.* **2005**, *88* (7), 1747−1753.

(39) Wolf, S. E.; Winterhalder, F. E.; Vibhu, V.; de Haart, L. G. J.; Guillon, O.; Eichel, R.-A.; Menzler, N. H. Solid Oxide Electrolysis Cells − Current Material Development and Industrial Application. *J. Mater. Chem. A* **2023**, *11* (34), 17977−18028.

(40) Li, N.; Verma, A.; Singh, P.; Kim, J.-H. Characterization of La0.58Sr0.4Co0.2Fe0.8O3−δ−Ce0.8Gd0.2O2 Composite Cathode for Intermediate Temperature Solid Oxide Fuel Cells. *Ceram. Int.* **2013**, *39* (1), 529−538.

(41) Lee, H.-K.; Hwang, J.-H. Electrical Properties in GDC (Gd_2O_3 -Doped CeO_2)/LSCF ($La_{0.6}Sr_{0.4}Co_{0.2}Fe_{0.8}O_3$) Cathode Composites for Intermediate Temperature Solid Oxide Fuel Cells. *J. Korean Ceram. Soc.* **2011**, *48* (1), 110−115.

(42) Railsback, J.; Choi, S. H.; Barnett, S. A. Effectiveness of Dense Gd-Doped Ceria Barrier Layers for (La,Sr)(Co,Fe)O3 Cathodes on Yttria-Stabilized Zirconia Electrolytes. *Solid State Ionics* **2019**, *335*, 74−81.

(43) Rembelski, D.; Viricelle, J. P.; Combemale, L.; Rieu, M. Characterization and Comparison of Different Cathode Materials for SC-SOFC: LSM, BSCF, SSC, and LSCF. *Fuel Cells* **2012**, *12* (2), 256−264.

(44) Jiang, S. P. A Comparison of O2 Reduction Reactions on Porous (La,Sr)MnO3 and (La,Sr)(Co,Fe)O3 Electrodes. *Solid State Ionics* **2002**, *146* (1), 1−22.

(45) Webb, S. M. SIXpack: A Graphical User Interface for XAS Analysis Using IFEFFIT. *Phys. Scr.* **2005**, *2005* (T115), 1011.

(46) Webb, S. M. MicroAnalysis Toolkit: X-ray Fluorescence Image Processing Software. In *AIP Conference Proceedings*; AIP Publishing, 2011. https://pubs.aip.org/aip/acp/article/1365/1/196/872092/The-MicroAnalysis-Toolkit-X-ray-Fluorescence-Image.

(47) van de Walle, A.; Ceder, G. Automating First-Principles Phase Diagram Calculations. *J. Phase Equilib.* **2002**, *23* (4), 348.

(48) van de Walle, A.; Asta, M. Self-Driven Lattice-Model Monte Carlo Simulations of Alloy Thermodynamic Properties and Phase Diagrams. *Model. Simul. Mater. Sci. Eng.* **2002**, *10* (5), 521.

(49) van de Walle, A.; Asta, M.; Ceder, G. The Alloy Theoretic Automated Toolkit: A User Guide. *Calphad* **2002**, *26* (4), 539−553.

(50) van de Walle, A. Multicomponent Multisublattice Alloys, Nonconfigurational Entropy and Other Additions to the Alloy Theoretic Automated Toolkit. *Calphad* **2009**, *33* (2), 266−278.

(51) van de Walle, A.; Tiwary, P.; de Jong, M.; Olmsted, D. L.; Asta, M.; Dick, A.; Shin, D.; Wang, Y.; Chen, L.-Q.; Liu, Z.-K. Efficient Stochastic Generation of Special Quasirandom Structures. *Calphad* **2013**, *42*, 13−18.

(52) Kresse, G.; Hafner, J. Ab Initio Molecular Dynamics for Liquid Metals. *Phys. Rev. B* **1993**, *47* (1), 558−561.

(53) Kresse, G.; Hafner, J. Ab Initio Molecular-Dynamics Simulation of the Liquid-Metal–Amorphous-Semiconductor Transition in Germanium. *Phys. Rev. B* **1994**, *49* (20), 14251−14269.

(54) Kresse, G.; Furthmüller, J. Efficiency of Ab-Initio Total Energy Calculations for Metals and Semiconductors Using a Plane-Wave Basis Set. *Comput. Mater. Sci.* **1996**, *6* (1), 15−50.

(55) Kresse, G.; Furthmüller, J. Efficient Iterative Schemes for Ab Initio Total-Energy Calculations Using a Plane-Wave Basis Set. *Phys. Rev. B* **1996**, *54* (16), 11169−11186.

(56) Blöchl, P. E. Projector Augmented-Wave Method. *Phys. Rev. B* **1994**, *50* (24), 17953−17979.

(57) Kresse, G.; Hafner, J. Norm-Conserving and Ultrasoft Pseudopotentials for First-Row and Transition Elements. *J. Phys.: condens. Matter* **1994**, *6* (40), 8245.

(58) Kresse, G.; Joubert, D. From Ultrasoft Pseudopotentials to the Projector Augmented-Wave Method. *Phys. Rev. B* **1999**, *59* (3), 1758−1775.

(59) Monkhorst, H. J.; Pack, J. D. Special Points for Brillouin-Zone Integrations. *Phys. Rev. B* **1976**, *13* (12), 5188−5192.

(60) Perdew, J. P.; Burke, K.; Ernzerhof, M. Generalized Gradient Approximation Made Simple. *Phys. Rev. Lett.* **1996**, *77* (18), 3865−3868.

(61) Dudarev, S. L.; Botton, G. A.; Savrasov, S. Y.; Humphreys, C. J.; Sutton, A. P. Electron-Energy-Loss Spectra and the Structural Stability of Nickel Oxide: An LSDA+U Study. *Phys. Rev. B* **1998**, *57* (3), 1505−1509.

(62) Jain, A.; Hautier, G.; Ong, S. P.; Moore, C. J.; Fischer, C. C.; Persson, K. A.; Ceder, G. Formation Enthalpies by Mixing GGA and GGA + U Calculations. *Phys. Rev. B* **2011**, *84* (4), 045115.

(63) Wang, L.; Maxisch, T.; Ceder, G. Oxidation Energies of Transition Metal Oxides within the GGA+U Framework. *Phys. Rev. B* **2006**, *73* (19), 195107.

(64) Chase, M. W.NIST-JANAF Thermochemical Tables. *J. Phys. Chem. Ref. Data*, 4th Ed., 1998; *9* 1745.

(65) Ong, S. P.; Wang, L.; Kang, B.; Ceder, G. Li−Fe−P−O2 Phase Diagram from First Principles Calculations. *Chem. Mater.* **2008**, *20* (5), 1798−1807.

(66) Haas, O.; Vogt, U. F.; Soltmann, C.; Braun, A.; Yoon, W.-S.; Yang, X. Q.; Graule, T. The Fe K-Edge X-Ray Absorption Characteristics of La1−xSrxFeO3−δ Prepared by Solid State Reaction. *Mater. Res. Bull.* **2009**, *44* (6), 1397−1404.

(67) Rowberg, A. J. E.; Slomski, H. S.; Kim, N.; Strange, N. A.; Gorman, B. P.; Shulda, S.; Ginley, D. S.; Kweon, K. E.; Wood, B. C. Impact of Sr-Containing Secondary Phases on Oxide Conductivity in Solid-Oxide Electrolyzer Cells. *Chem. Mater.* **2024**, *36* (13), 6464−6474.

(68) Zhang, W.; Barfod, R. *Investigation of Degradation Mechanisms of LSCF Based SOFC Cathodes — by CALPHAD Modeling and Experiments*; Department of Energy Conversion and Storage, Technical University of Denmark, 2012.

(69) Darvish, S.; Gopalan, S.; Zhong, Y. Thermodynamic Stability Maps for the La0.6Sr0.4Co0.2Fe0.8O3±δ−CO2−O2 System for Application in Solid Oxide Fuel Cells. *J. Power Sources* **2016**, *336*, 351−359.

(70) Darvish, S.; Wang, C. C.; Jiang, S. P.; Zhong, Y. Thermodynamic Stability Mapping and Electrochemical Study of La1-xSrxCo0.2Fe0.8O3±δ (X = 0.2−0.4) as a Cathode of Solid Oxide Fuel Cells in the Presence of SO2. *Electrochim. Acta* **2018**, *287*, 68−77.